PCCP
Physical Chemistry Chemical Physics

Accepted Manuscript

This article can be cited before page numbers have been issued, to do this please use: R. Zhang, A. Chutia, A. A. Sokol, D. Chadwick and C. R. A. Catlow, *Phys. Chem. Chem. Phys.*, 2021, DOI: 10.1039/D1CP02973H.

ROYAL SOCIETY OF CHEMISTRY

rsc.li/pccp

View Article Online
DOI: 10.1039/D1CP02973H

A computational investigation of the adsorption of small copper clusters on the CeO_2(110) surface

Rui Zhang[(1)*], Arunabhiram Chutia[(2)*], Alexey A. Sokol[(3)], David Chadwick[(1)], C. Richard A. Catlow [(3),(4)]

1. Dept of Chemical Engineering, Imperial College London, South Kensington Campus, London SW7 2AZ, UK
2. School of Chemistry, University of Lincoln, Lincoln LN6 7TS, UK
3. Dept of Chemistry, University College London, 20 Gordon St., London WC1H 0AJ, UK
4. School of Chemistry, Cardiff University, Park Place, Cardiff CF10 1AT, UK

1. Abstract

We report a detailed density functional theory (DFT) study of the geometrical and electronic properties, and the growth mechanism of a Cu_n (n=1-4) cluster on a stoichiometric, and especially on a defective CeO_2(110) surface with one surface oxygen vacancy, without using pre-assumed gas-phase Cu_n cluster shapes. This gives new and valuable theoretical insight into experimental work regarding debatable active sites of promising CuO_x/CeO_2-nanorod catalysts in many reactions. We demonstrate that CeO_2(110) is highly reducible upon Cu_n adsorption, with electron transfer from Cu_n clusters, and that a Cu_n cluster grows along the long bridge sites until Cu_3, so that each Cu atom can interact strongly with surface oxygen ions at these sites, forming stable structures on both stoichiometric and defective CeO_2(110) surface. Cu-Cu interactions are, however, limited, since Cu atoms are distant from each other, inhibiting the formation of Cu-Cu bonds. This monolayer then begins to grow into a bilayer as seen in the Cu_3 to Cu_4 transition, with long-bridge site Cu as anchoring sites. Our calculations on Cu_4 adsorption reveal a Cu bilayer rich in Cu^+ species at the Cu-O interface.

2. Introduction

Ceria-based catalysts have been widely studied in the past thirty years [1, 2], stimulated by their successful applications, for example as a promoter in the automotive three-way catalysts (TWCs) [3]. Ceria (CeO_2) crystals have a face-centred cubic fluorite structure, characterised by three low-index facets (100), (110), and (111). The material has a high oxygen storage capacity (OSC) as it can easily shift between Ce^{4+} and Ce^{3+}, forming bulk and surface oxygen vacancies with consequent high reducibility [4], which is further enhanced in well-defined ceria nanostructures, such as nanoparticles, nanorods, and nanocubes which expose (111), (110)/(100), and (100) surfaces, respectively [5-7]. Consequently, nanostructured ceria-based catalysts, such as CuO_x/CeO_2 catalysts, are active in many reactions, for example, the water gas shift (WGS) reaction [8, 9] and CO oxidation [10, 11].

The structure and properties of CuO_x/CeO_2 catalysts have been widely studied. Chen *et al.* used high angle annular dark field scanning transmission electron microscope (HAADF-STEM) and *in situ* infra-red spectroscopy, as well as density functional theory (DFT) calculations to provide experimental and theoretical evidence of a Cu bilayer on a $CeO_2(111)$ surface [8]. A top layer of Cu^0 atoms were bonded with a bottom layer of mainly Cu^+ ions, which in turn were bonded with surface oxygen vacancies (in a Cu^+-O_v-Ce^{3+} form). This copper-ceria interfacial perimeter was identified as the active site for WGS. Kang *et al.* recently reported experimental and theoretical evidence of an active atomic $[Cu(I)O_2]^{3-}$ site for CO oxidation which dynamically changed to/from $[Cu(II)O_4]^{6-}$ via an electrophilic $[Cu(II)O_2(\eta^2\text{-}O_2)]^{4-}$ intermediate on the $CeO_2(111)$ surface, both of which had a lower HOMO energy compared to Cu clusters on the surface [10].

Besides these combined experimental and theoretical studies, there are several computational studies focusing mainly on the atomic and electronic structures of $Cu/CeO_2(111)$ (since $CeO_2(111)$ is the most stable surface [12]), employing density functional theory (DFT), commonly the DFT+*U* approach, in which an effective Hubbard U_{eff} parameter is used to consider on-site Coulomb repulsions. For example, Szabová *et al.* reported their most stable Cu/CeO_2 structure with one oxidised Cu^+ and one reduced surface Ce^{3+} furthest away from the Cu^+, with the nearest neighbour surface oxygen ions bonding closely with the Cu^+ [13]. For a Cu/CeO_{2-x} system, the Cu atom sited above an oxygen vacancy was reduced to $Cu^{\delta-}$. Cu adsorption on surface oxygen vacancies was reported less stable than on a stoichiometric surface, suggesting that Cu nucleation was unlikely on the reduced $CeO_2(111)$ surface. Yang *et al.* calculated that small Cu_n (n=1-4) clusters bonding with surface oxygen ions on a stoichiometric $CeO_2(111)$ surface, are positively charged and slightly polarised, showing shortened Cu-O distances [14]. Cu_2 and Cu_3 adopted a planar shape, while the two-dimensional (2D) to 3D structural transition was predicted in a Cu_4 cluster, because of the comparable strengths of Cu-Cu and Cu-O interactions. Paz-Borbon *et al.* calculated planar geometries of all Cu_n (n=1-5) clusters on a stoichiometric $CeO_2(111)$ surface, due to strong Cu-O interactions and charge transfer effects [15]. The number of surface Ce^{3+} ions increased with the Cu cluster size, with a maximum of three electrons transferred from a Cu_5 cluster. Regarding ceria surface oxygen vacancies, Jerratsch *et al.* investigated Ce^{3+} localisation on a defective $CeO_2(111)$ surface with a single oxygen vacancy [16]. They found at least one Ce^{3+} ion was not the nearest neighbour (NN) to the vacancy from both DFT calculations and scanning-tunnelling microscopy (STM).

Recently, Ning *et al.*, based on a detailed H_2-temperature programmed reduction (H_2-TPR) and X-ray photoelectron spectra (XPS) study, reported that different ceria shapes (particles, rods, and cubes) significantly affected the dispersion and chemical properties of copper

species of a CuO/CeO_2 catalyst, [11]. They observed CuO_x mono- and bilayer (using HAADF-STEM) as the dominant species, particularly on ceria nanorods, which were rich in Cu^+ at the copper-ceria interface (Cu-[O_x]-Ce). The CuO/CeO_2-nanorod catalyst had the highest concentration of surface Cu^+ and oxygen vacancies, and thus showed a higher activity in CO oxidation, compared to catalysts with other shapes. Their experimental results strongly suggest that CuO_x mono- and bilayer are likely to form on CeO_2(110) and the copper-ceria interface may be rich in Cu^+ and oxygen vacancies. These atomic and electronic features are important for CO oxidation [17], as well as many more reactions such as CO_2 hydrogenation to methanol [18], N_2O decomposition [6], WGS [9], and NO reduction [19].

As CeO_2(110) is less stable than CeO_2(111), Cu/CeO_2(110) is less studied. A number of computational studies are, however, reported. As with Cu adatom adsorption on CeO_2(111), a DFT study of Nolan suggested a Cu^+ ion and a Ce^{3+} ion on a CeO_2(110) surface with significant local distortion [20]. Cui *et al.* found a Cu^+ or a Cu^{2+} ion on CeO_2(110) when locating the Cu adatom at different adsorption sites [21]. Recently, Chutia *et al.* studied in detail the geometric and electronic properties of a Cu adatom adsorbed at different sites on CeO_2(110) [22]. They found the O_{top} initial structure (Cu on top of a surface O ion) led to the most stable optimised structure, where the Cu was at an O-Ce-O long bridge site, showing one electron transfer and strong Cu-O interactions. Ren *et al.* later studied the growth mechanism of a Cu_n (n=1-5) cluster on CeO_2(110) [23]. They observed a planar rhombus $Cu_{4\text{-}p}$ cluster transforming to a 3D tetrahedral $Cu_{4\text{-}t}$ cluster on the surface, and thus identified Cu_3 as a critical size in Cu nucleation, which however was not favourable on CeO_2(110). For a defective CeO_2(110) surface, the modelling study of Kullgren *et al.* reported that the most stable structure had an asymmetrical bridge site, in which one nearest surface oxygen moved towards the vacancy, bridging two nearby surface Ce species, and the Ce^{3+} ions were localised at an NN and NNN (next-nearest neighbour) position, respectively [24].

Considering debatable active sites of promising CuO_x/CeO_2-nanorod catalysts in many reactions [8, 10, 11, 17, 18], being it Cu species with different oxidation states, or the Cu-ceria interface, the understanding of atomic and electronic properties of small Cu clusters, a CuO_x mono- and bilayer on CeO_2(110), especially on a defective surface and at the copper-ceria interface, is thus of great interest and importance. However, there is a lack of comprehensive study of small Cu cluster morphologies and electronic interactions with CeO_2(110) surface. Therefore, in this study, we have conducted systematic DFT calculations to investigate the atomic and electronic properties, and the growth mechanism of a Cu_n (n=2-4) cluster on a stoichiometric, and especially on a defective CeO_2(110) surface with one surface oxygen vacancy, growing from a Cu_{n-1} cluster with an additional Cu atom placed at different adsorption sites. Our detailed investigation of small Cu_n (n=1-4) cluster adsorption on CeO_2(110), without using pre-assumed gas-phase Cu_n cluster shapes, provides fundamental understanding of highly reducible CeO_2(110) surface upon Cu_n adsorption, and strong Cu-surface oxygen interactions with/out a surface oxygen vacancy, being the predominating factor in Cu_n (n=1-4) cluster growth on CeO_2(110), with relevance to experimental studies of CuO_x/CeO_2-nanorod catalysts. In the next section we present the theoretical methods employed, which we follow by the results and discussion first of Cu_n adsorption on a stoichiometric surface, and then on a defective surface. Our study leads to detailed and valuable understanding of structural and electronic properties of a Cu_n (n=1-4) cluster adsorbed on stoichiometric and defective CeO_2(110) surface, giving theoretical insights into the development of atomistic and electronic properties of a CuO_x mono/bilayer at the Cu-O interface on CeO_2(110).

3. Computational Details

The Vienna Ab initio Simulation Package (VASP) was used to perform all the periodic spin-polarised DFT+*U* calculations [25-27]. Blöchl's projector augmented wave (PAW) method was used to describe the core electrons of all atoms [28]. The cut-off energy for the expansion of the plane-wave basis sets was set to 550 eV, with bulk energies converged to within 10^{-5} eV. A convergence criterion of 0.01 eV $Å^{-1}$ was chosen for structural optimisation. The Perdew-Burke-Ernzerhof (PBE) version of the generalised gradient approximation (GGA) was used to carry out geometry optimisation and total energy calculations [29]. The pristine CeO_2 (110) surface was modelled by a 3x3 supercell with 7 atomic layers in which the bottom four layers were fixed to mimic the bulk of the system. The slab was cut from the bulk CeO_2 with a theoretical lattice constant of 5.492 Å, which is close to the experimental value of 5.411 Å. In the direction perpendicular to the surface, a vacuum gap of ~18 Å was used. In all the calculations, Cu adsorption was only allowed on one of the two surfaces. Therefore, the dipole moment, due to Cu_n cluster adsorption, was corrected by using the methods proposed by Makov *et al.* and Neugebauer *et al.* as implemented in VASP [30, 31]. A 2x2x1 *k*-point sampling grid was employed in all slab calculations, using the Monkhorst-Pack scheme [32]. A Hubbard parameter *U* [33-35] in the Dudarev correction form [35, 36] was added to the energy functional, to correct the self-interaction error due to Ce localised 4*f*-orbital electrons. In this study, a U_{eff} value of 5.0 eV was employed for both Ce 4*f*-orbitals [14, 20, 22, 23] and Cu 3*d*-orbitals [22, 37], which could correctly represent electron localisation in Ce 4*f* and Cu 3*d* orbitals, respectively. A single Cu atom and a Cu_2 cluster in the gas phase were simulated using a 20x20x20 $Å^3$ cubic cell.

A two-stage optimisation procedure, originally proposed by Grau-Crespo [38-40] was used to localise electrons in Ce 4*f* orbitals during CeO_2(110) surface reduction, as the localisation is effected by lattice relaxation around the Ce^{3+} which is the response to the lower charge and larger radius of the Ce^{3+} compared with Ce^{4+}. To generate this relaxation field Ce ions were replaced with larger La atoms. After geometry optimisation, the La atoms were then replaced by Ce atoms, which now have the appropriate surrounding relaxed configuration needed to localise an electron at the Ce site; the system is then fully geometry optimised.

Bader charges of different atoms were obtained by using the modified Bader charge analysis implemented by Tang *et al.* [41]. The Visualisation for Electronic and STructural Analysis (VESTA) package [42] was employed to visualise different structures and spin densities.

The adsorption energy per Cu atom, E_{ad} of any given Cu_n/CeO_2(110) structure was calculated as follows,

$$E_{\mathrm{ad}} = \frac{E(\mathrm{Cu}_n/\mathrm{CeO}_2) - nE(\mathrm{Cu}_1) - E(\mathrm{CeO}_2}{n} \quad 1$$

where $E(\mathrm{Cu}_n/\mathrm{CeO}_2)$ is the energy of an optimised Cu_n/CeO_2(110) structure, $E(\mathrm{Cu}_1)$ is the energy of a single Cu atom in the gas phase, $E(\mathrm{CeO}_2)$ is the energy of a relaxed/optimised stoichiometric CeO_2(110) surface, and n is the number of Cu atoms. In this definition, more negative adsorption energies imply stronger, more favourable adsorption.

For the calculations involving reduced surfaces, the oxygen vacancy formation energy E_{v} was calculated as follows,

$$E_{\mathrm{v}} = E(\mathrm{CeO}_{2\mathrm{v}}) + \frac{1}{2}E(\mathrm{O}_2) - E(\mathrm{CeO}_2) \quad 2$$

where $E(\mathrm{CeO}_{2\mathrm{v}})$ is the energy of a relaxed/optimised defective CeO_2(110)-Ov surface with one oxygen vacancy, and $E(\mathrm{O}_2)$ is the energy of a ground-state oxygen molecule in the gas phase.

Eq. 1 was also applied for the adsorption energy calculation of the Cu_n/CeO_2(110)-Ov systems, where the energy of an optimised Cu_n/CeO_2(110)-Ov structure and a relaxed/optimised defective CeO_2(110)-Ov

surface were used instead of the energy for the stoichiometric surface.

The charge density difference, ρ_{diff}, was calculated by subtracting the sum of the charge densities of a Cu_n cluster (ρ_{Cu_n}) and the ceria surface (ρ_{ceria})) of the same geometry as the system from the total charge density of the system (ρ_{sys}), which is shown as follows.

$$\rho_{\mathrm{diff}} = \rho_{\mathrm{sys}} - (\rho_{\mathrm{Cu}_n} + \rho_{\mathrm{ceria}}) \qquad 3$$

4. Results and Discussion

4.1 Adsorption of Cu on CeO_2(110) surface

We first reproduced the atomic and electronic investigation of a Cu adatom adsorbed on CeO_2(110) at four different adsorption sites [22], *i.e.* on top of a surface Ce atom (Ce_{top}), a surface O atom (O_{top}), the middle of a surface four-fold hollow site (four-$fold_{hollow}$) and the middle of a surface O-Ce short bridge site (O-$Ce_{short\ bdg}$). In the optimised structure having the most negative Cu adsorption energy of -3.258 eV, the Cu atom is close to the surface and bonded with two surface O ions on top of a second-layer Ce ion (named as an O-Ce-O long bridge site), which agrees with earlier work [21, 22]. Results and detailed discussion can be found in ESI Section 1.1.

4.2 Adsorption of Cu_2 on CeO_2(110) surface

A Cu_2 cluster with a Cu-Cu distance of 2.42 Å was placed either around an O-Ce-O long bridge site (Conf1-5) or on top of a second-layer four-fold hollow site (Conf6-7), parallel or perpendicular to the CeO_2(110) surface, producing seven initial structures, illustrated in Fig. 1. The O-Ce-O long bridge site was the most stable adsorption site, as found in Section 4.1, therefore, this site and the associated second-layer four-fold hollow site were chosen.

Local surface distortion around the Cu_2 cluster is observed in all optimised structures (see Fig. 2), also indicated by the average surface Ce-O bond lengths which are slightly larger than that of a pristine surface (2.342 Å), as listed in Table 1. Only Conf4 and Conf7 show significant structural changes from their corresponding initial structures. For Conf4, the two Cu atoms are bonded with nearby surface O ions at two long bridge sites, respectively, which were initially placed at one long bridge site. The optimised structure of Conf7 is essentially the same as that of Conf4 despite the Cu_2 cluster being initially perpendicular to the surface, indicating that formation of a linear Cu_2 cluster parallel and close to the surface is favoured. The optimised Conf7 has the most negative Cu adsorption energy, followed by Conf4, Conf1, Conf5, Conf3, Conf2 and Conf6. Therefore, only the most stable Conf7 and metastable Conf4 and 1 are discussed here.

Conf7, 4, and 1 have similar optimised structures, *i.e.* two Cu atoms bonded at two long bridge sites [23], in which the number of surface O ions available for Cu-O binding is maximised, showing short Cu-O distances in the range of 1.8-1.9 Å (see Table 1) and the most negative adsorption energies at -3.492, -3.367, and -2.810 eV, respectively.

In terms of electronic structures, Conf7, 4, and 1 have two electrons transferred from the Cu_2 cluster to the surface, illustrated by the spin density isosurfaces of two reduced Ce^{3+} ions, Fig. 2, also their distinct magnetic moments in opposite spins (M_{Ce}, Table 1), and their Cu_2 total magnetic moment being 0.

Different Ce^{3+} localisation has an impact on the Cu adsorption energy of Conf7, 4 and 1. In Conf7 and 4, the two Ce^{3+} ions are located at two different surface four-fold hollow sites, opposite to each other, which enables nearby oxygen ions to bind strongly with the Cu atoms, thus stabilising the structure. Differently, in Conf1, the two Ce^{3+} ions are on the same four-fold hollow site. Since a Ce^{3+} ion has a larger radius than a Ce^{4+} ion, the two Ce^{3+} ions move slightly away from each other, stretching Ce-O bonds and thus limiting movement of the bridging O ion towards its nearest Cu atom.

Besides, slightly different Cu-O interactions of Conf7 and 4 also affects their adsorption

energies, though they have similar geometry and Ce^{3+} localisation. A detailed PDOS analysis was conducted, focusing on orbital interactions between one of the Cu atoms and its bonded three O ions (labelled as O1, O2, O3, in ESI Fig. 7). Conf7 and 4 show similar overall signatures (including Cu 4*s*, 3*p* and 3*d*, O 2*s* and 2*p*), Fig. 7 a-b. They also demonstrate a noticeable overlap between Cu 3*d* and O 2*p* orbitals in the range of -6 to -5 eV, which is shown in more detail by PDOS plots of this Cu and its nearest O ion, ESI Fig. 7 c-d. Additionally, a comparison of the 3*d* signatures of the Cu_2 cluster before (ESI Fig. 8 a) and after adsorption shows that they are broader in Conf7 as compared to Conf4. Further to this the number of states of O 2*p* signature in the range of -2 to 0 eV is larger in Conf7 than in Conf4, indicating stronger Cu-O interactions, which suggests why Conf7 has a slightly more negative adsorption energy. The strong Cu-O interactions are also confirmed by a deeper energy of Cu 3*d* and O 2*p* orbitals in both configurations than that of Cu 3*d* in a gaseous Cu_2 cluster and O 2*p* on a pristine CeO_2(110) surface (see ESI Fig.8 b).

For other configurations with less negative adsorption energies (see ESI Section 1.2), the observed weakening in adsorption energies of these configurations is seen to correlate with the decrease in Cu-Cu bond lengths, suggestive of a Coulomb repulsion between Cu atoms in sterically constrained structures. Partial oxidation of Cu_2 to a top $Cu^{\delta-}$ and a bottom Cu^{2+} species (Conf3) or two $Cu^{\delta+}$ (Conf2), and partial reduction of Ce^{4+} to Ce^{3+} [21] (Conf6), also suggest electronic structures affecting Cu adsorption energy.

Overall, we find the configuration with the most negative adsorption energy showing two Cu adsorbed at two adjacent long bridge sites, and intriguingly complex electronic structures with varied interactions between Cu species and between Cu and surface ions at different positions.

4.3 Adsorption of Cu_3 on CeO_2(110) surface

The two stable structures from the Cu_2/CeO_2(110) system with small adjustments were used to construct eight initial Cu_3/CeO_2(110) configurations. The third Cu was placed at different adsorption sites on the surface with respect to the Cu_2 cluster at different heights from the surface (Fig. 3).

All optimised structures show surface distortion around the Cu atoms, as illustrated in Fig. 4, also shown by the average surface Ce-O bond lengths being larger than that of a pristine surface, as noted in Table 2. The optimised Conf3, 2, and 1 show a linear Cu_3 structure [23] and the most negative adsorption energies of -3.429 eV, -3.t318 eV, and -3.307 eV, respectively. This is because the three Cu atoms are adsorbed at three adjacent long bridge sites, enabling them to bond strongly with at least two nearby surface O ions, showing short Cu-O distances in the range of 1.75-1.90 Å, Table 2, which agree with the calculated values reported by Chutia *et al*., yet smaller than their experimentally measured values of 1.9-2.4 Å [22]. Cu-Cu interactions are weak since Cu atoms are far apart, hardly interacting, except in Conf3. This additional Cu-Cu bond (2.463 Å) thus leads to the most negative Cu adsorption energy of Conf3.

We note that Ren *et al.* also calculated the adsorption energy per Cu atom of a Cu_3 linear cluster (-1.69 eV) on CeO_2(110), which was greater than that of a Cu_3 triangle cluster (-1.53 eV); yet with a difference of more than 1 eV in absolute values from ours, could that have resulted from different model parameters used, such as supercell size, cut-off energy, force convergence criteria, and k-point sampling [23].

The most stable Conf3, and metastable Conf2 and 1, have three electrons transferred from Cu_3 to the surface, as illustrated by the spin density isosurfaces around three reduced Ce^{3+} ions, Fig. 4.

Other configurations have a Cu_3 triangle adsorbed on the surface, thus resulting in weak copper-surface oxygen interactions, and weak

electronic interactions (see ESI Section 1.3), and consequently less negative adsorption energies.

The $Cu_{1-3}/CeO_2(110)$ configurations with the most negative Cu adsorption energies suggest that, with an increasing Cu loading, a Cu monolayer grows along the long bridge sites upon Cu adsorption, demonstrated by a Cu adatom growing to a Cu_2, and a linear Cu_3 cluster at the long bridge sites, agreeing with previous work [23]. Our extensive examination of different initial configurations of Cu_n adsorbed at various adsorption sites, and associated detailed electronic structure investigation, provide insights into the impact of surface Cu-O and Cu-Cu interactions on optimised structures and adsorption energies.

4.4 Adsorption of Cu_4 on $CeO_2(110)$ surface

Eight initial structures were constructed based on a stable linear Cu_3 cluster and a triangular cluster from the $Cu_3/CeO_2(110)$ system. The fourth Cu atom was placed at different adsorption sites with respect to the Cu_3 cluster and at different heights above the surface, Fig. 5.

All optimised structures show surface distortion around the Cu atoms, as illustrated in Fig. 6, also shown by the different values of average surface Ce-O bond length from that of a pristine surface, as listed in Table 3. Conf3, 4, and 1 have the most negative Cu adsorption energies at -2.971, -2.961, and -2.918 eV, respectively, followed by Conf2, Conf7, Conf8, Conf6 and Conf5, Table 3. Therefore, only the former three are discussed here (see ESI Section 1.4 for more details).

In Conf3 and 4, there is an isolated Cu bonded at a long bridge site, and a Cu_3 cluster bonded at two adjacent long bridge sites. In Conf3, the fourth Cu is raised above the surface to bond with two Cu and one O ion, while in Conf4, the fourth Cu atom moves down slightly towards the surface, bonding with one second-layer and one surface O ion, and two nearest Cu atoms. In Conf1, the four Cu atoms are distributed at three adjacent long bridge sites, *i.e.* two isolated Cu at two long bridge sites, and a Cu_2 cluster at one long bridge site. The fourth Cu atom moves from the Ce_{top} site towards and bonds with the nearest surface O ion and one nearby Cu. The strong copper-surface interactions in Conf3, 4, and 1 thus contribute to their most negative adsorption energies.

From a Cu_3 to a Cu_4 cluster, the close competition between Cu-O and Cu-Cu interactions within a limited space leads to a Cu monolayer to bilayer transition along the adjacent long bridge sites. The small energy difference between Conf3, 4, 1, and 2 (maximum of 0.11 eV) and their different structures suggest that a Cu bilayer can start growing from several configurations. The stable and especially interesting optimised structure of Conf4, with one of the Cu atoms incorporated into the surface, is also observed experimentally [19, 43].

Conf2 has an adsorption energy very close to Con1, yet, it only has three electrons transferred, showing interesting electronic features in relevance to catalytic reactions. Its Cu 4*s* orbital PDOS plots, ESI Fig. 14, a-c, suggest that the bottom three Cu atoms each donate one electron to the surface, becoming a Cu^+ ion. Interestingly, the top Cu has two 4*s* electrons in opposite spins (a pair of distinct 4*s* signatures below E_F), forming a $Cu^{\delta-}$ species with a Bader charge of -0.437 e. This extra electron appearing in the top Cu 4*s* orbital originates from the bottom two Cu atoms with spin density isosurfaces, Fig. 6. In the plots of their 3*d* orbital PDOS, ESI Fig. 15, we note each has one unoccupied down-spin signature above E_F, suggesting the electron in the top Cu is partially from these two bottom Cu 3*d* orbitals, though the contribution from the bottom Cu furthest away from the top is larger. Since this Cu is coordinated with three O ions, it can be easily stabilised as a Cu^{2+} ion, with a Bader charge of 0.724 e [21]. As Conf2 and 3 have similar energies, electrons can easily exchange between Cu ions on $CeO_2(110)$, *i.e*. shift

between Cu^{+} and Cu^{2+}, which has been reported as providing active sites for many reactions [6, 10, 17].

Paz-Borbón *et al.* showed a maximum of two electrons transferred from a Cu_4 cluster to CeO_2(111) [15], whereas in our study, 2-4 electrons are transferred to CeO_2(110). This significant difference in the number of electrons transferred suggests CeO_2(110) could be more easily reduced after Cu cluster adsorption.

To investigate other additional possible electron transfers from Cu_4 to CeO_2(110), the initial structure of Conf4 was used to set up new structures, in which 1-3 pre-assumed Ce^{3+} ions were replaced with 1-3 La ions, respectively, for geometry optimisation. These La ions were then replaced by Ce ions for final optimisation. It was only possible to observe three electrons transferred, in one structure (labelled as Conf4-2, detailed discussion in ESI Section 1.4), whereas in the other two, four electrons were still transferred.

From the above discussion, we can conclude that CeO_2(110) is highly reducible upon Cu_4 adsorption, and competing Cu-Cu and Cu-O interactions are important in determining Cu_4 shape and energetics, and electronic structure of Cu_4/CeO_2(110). Long-bridge site Cu atoms were the anchoring sites for Cu_3 growth to Cu_4.

4.5 Adsorption of Cu and Cu_2 on CeO_2(110) surface with one oxygen vacancy

CeO_2(110) with one oxygen vacancy

To investigate the impact of surface oxygen vacancies on geometric and electronic properties of a Cu_n/CeO_2(110) (n=1-4) structure, and on Cu-O and Cu-Cu interactions, we removed the same topmost-layer oxygen from different Cu_n/CeO_2(110) initial structures before geometric and electronic optimisation.

An optimised defective CeO_2(110) surface with one surface oxygen vacancy (CeO_2(110)-Ov) is chosen as the new baseline for adsorption energy calculations when absorbing different Cu clusters on such a defective surface.

We thus first removed one oxygen from CeO_2(110) (see Fig. 7.0) and set up three configurations with different combinations of two pre-assumed Ce^{3+} sites around the oxygen vacancy, which are clearly illustrated in the optimised structures, Fig. 7 1-3. In Case1, the two surface Ce^{3+} ions are nearest neighbours (NN) of the vacancy. In Case2, one Ce^{3+} is a surface NN, while the other is a second-layer next nearest neighbour (NNN) of the vacancy. In Case3, one Ce^{3+} is a surface NN, while the other one is a surface NNN.

In Case1, the nearest surface oxygen ion moved towards the vacancy on the surface plane. It bonds with two Ce^{3+} ions with equal Ce^{3+}-O bond lengths (2.341 Å). There is no significant surface distortion, as indicated by an average surface Ce-O distance of 2.381 Å, closest to the value of a stoichiometric surface, unlike in the other two cases, possibly because of the hindrance to relaxation of two adjacent large Ce^{3+} ions locally [24]. In Case2, the nearest oxygen ion moves towards the vacancy significantly. It is slightly raised from the surface, bridging one Ce^{3+} and one Ce^{4+} ion. Since a Ce^{3+} ion has a larger radius than a Ce^{4+} ion, the Ce^{3+}-O bond is longer than the Ce^{4+}-O bond, forming an asymmetric bridge site [24]. A similar asymmetric bridge site is also observed in Case3.

Calculated oxygen vacancy formation energies are in the range of 0.98-1.43 eV, as reported in Table 4, which are slightly lower than those from previous work (1.54-2.69 eV) [2, 24, 44-46], because of a more negative O_2 binding energy of -9.863 eV (bond length 1.233 Å) used in our work [24, 47] (ESI Section 1.5). The well-known error of overbinding O_2 using GGA/LDA DFT and PAW potentials [24, 46], as well as different computational parameters used (*e.g.* supercell size, cut-off energy, U value, etc.) make it difficult to compare absolute values with earlier work; however the relative comparison between Case1 to 3 is not affected. Case3

shows the smallest oxygen vacancy formation energy, followed by Case1 and 2, which suggests it is energetically favourable to form surface rather than second-layer Ce^{3+} ions [24, 46]. An NN-NNN Ce^{3+} pair combination (Conf3) is more stable than a NN-NN combination (Conf1), suggesting it is favourable to coordinate a Ce^{3+} ion with Ce^{4+} ions rather than Ce^{3+} ions [24]. Therefore, Case3 is chosen as the new baseline for Cu adsorption energy calculations.

Cu/CeO_2(110) with one oxygen vacancy

The initial structure of O_{top} was chosen and the surface oxygen on the topmost layer directly under the Cu adatom was removed (see Fig. 8.0). Two cases were set up with different locations of three pre-assumed Ce^{3+} ions.

Case1 and 2 show similar optimised structures, in which the Cu atom is located at a long bridge site, bonding with two surface O ions, as illustrated in Fig. 8. These two structures are similar to the optimised O_{top} structure, as shown in ESI Fig. 2.2. Because of the additional Cu-O interaction, the nearest surface O ion moved even closer to the vacancy and formed a Cu-O bond, compared to that in a defective CeO_2(110) surface without Cu adsorption.

In both cases, there are three electrons trapped in three Ce^{3+} 4*f* orbitals, *i.e.* one from the Cu adatom, and two from the oxygen vacancy. However, their electronic structures are quite different. In Case1, there is one surface and one second-layer NN Ce^{3+} of the vacancy, and one surface NNN Ce^{3+}. In Case2, there are two NN Ce^{3+} ions and one NNN Ce^{3+} ion, all of which are on the surface. Case2 has a slightly more negative adsorption energy at -3.690 eV, since it is energetically more favourable to form surface Ce^{3+} ions than second-layer Ce^{3+} ions. The shorter Cu-O distance of Case2 also contributes to its higher stability. Electron transfer is also confirmed by magnetic moments of these species, as listed in Table 5.

Cu_2/CeO_2(110) with one oxygen vacancy

The initial structure of Conf1 and 4 from the Cu_2/CeO_2(110) system were chosen to create one surface oxygen vacancy, respectively, seen in Fig. 9, since optimised Conf1 and 4 have the most negative Cu adsorption energies.

In optimised Conf1v and 4v, shown in Fig. 9, the nearest surface oxygen ion moved very close to the vacancy, bonding to one of the Cu atoms. These two structures are very similar to the optimised Conf1 and 4 with a stoichiometric surface, although the Cu_2 cluster bonds with the nearest oxygen ion of the vacancy instead of the oxygen ion originally at the vacancy.

Both Conf1v and 4v have four electrons localised at four Ce^{3+} ions. In Conf1v, all four Ce^{3+} ions are on the surface, *i.e.* two NNs and two NNNs of the vacancy. In Conf4v, there are two surface NNs, one second-layer NN, and one second-layer NNN, which introduces more structural perturbation to the surface, as suggested by a much smaller value of average surface Ce-O bond length (2.317 Å), compared to that of Conf1v (2.360 Å). As a result, Conf1v shows a more negative Cu adsorption energy of -3.356 eV than Conf4v (-3.207 eV). The stronger Cu-O bonding with a shorter Cu-O distance also contributes to the more negative adsorption energy of Conf1v. Electron transfer is also confirmed by the magnetic moments of these species, reported in Table 5.

4.6 Adsorption of Cu_3 on CeO_2(110) surface with one oxygen vacancy

The initial structure of Conf2, 3, 6 and 7 from the Cu_3/CeO_2(110) system were chosen to create one surface oxygen vacancy (see Fig. 10), whose optimised structures show stable linear Cu_3 clusters and two types of unstable triangular Cu_3 clusters, respectively.

Conf2v has the most negative Cu adsorption energy of -3.350 eV, because of strong Cu-O interactions. It is the only optimised structure showing a linear Cu_3 cluster (see Fig. 10), similar to that of Conf2 with a stoichiometric surface. Surface oxygen ions on the same side

as the vacancy are raised from the surface and bond closely with the Cu_3 cluster, showing short Cu-O distances (Table 6), which include the nearest surface oxygen ion which moves close to the vacancy. Conf7v, 6v, and 3v have weaker Cu adsorption, showing one Cu far away from the surface, without Cu-surface O binding, as a result of weakened Cu-O interactions due to vacancy formation (ESI Section 1.6).

In Conf2v, there are five electrons trapped in Ce^{3+} 4*f* orbitals, whereas in Conf3v, 6v and 7v, only three electrons are trapped, and the other two electrons are found to locate in the Cu_3 cluster (discussion in ESI Section 1.6).

From the $Cu_{1-3}/CeO_2(110)$-Ov configurations with the most negative Cu adsorption energies, we could again conclude a Cu monolayer growth pattern along the long bridge sites after Cu adsorption, which is essentially the same as that on a stoichiometric surface. Both surface and second-layer Ce^{3+} ions are formed, but the latter are energetically less favoured.

4.7 Adsorption of Cu_4 on $CeO_2(110)$ surface with one oxygen vacancy

The initial structures of Conf2, 3, 4, and 7 from the $Cu_4/CeO_2(110)$ system were chosen to create one surface oxygen vacancy, Fig. 11, whose optimised structures demonstrate unique features and represent both stable and unstable configurations.

Conf4v has the most negative Cu adsorption energy of -2.674 eV, tightly followed by Conf3v, Conf7v, and Conf2v, Table 6, whose geometric and electronic structures discussed in detail in ESI Section 1.7. The optimised Conf4v is different from Conf4 with a stoichiometric surface, as a result of weakened Cu-O interactions. The fourth Cu in Conf4v moves away from the surface and bonds with two Cu and one O ion, whereas in Conf4, it moves down towards the surface and bonds with two Cu and both surface and second-layer O ions.

In Conf4v, five surface Ce^{4+} ions are reduced to Ce^{3+}, whereas four Ce^{4+} ions are reduced on the surface in the other structures. Clearly, the most negative adsorption energy of Conf4v can be related to the greatest number of reduced Ce^{3+} ions on the surface. The Cu_4 total magnetic moment is -0.409 μ_B, taking *s*, *p* and *d* orbitals into account. The two middle Cu atoms show a spin density isosurface around them, Fig. 11, and their 4*s* PDOS plots show two 4*s* signatures with similar magnitude below E_F (see ESI Fig. 23). These observations suggest that three electrons are transferred from Cu_4 to the surface, and one shared between the middle two Cu atoms, thus forming two Cu^+ ions with Bader charges of 0.470 and 0.598 e, and two $Cu^{\delta+}$-$Cu^{\delta-}$ species with Bader charges of 0.361 and -0.231 e. Similarly, in Conf2v, 3v, and 7v, three $Cu^{\delta+}$-Cu^0 species and one Cu^+ ion are formed on the surface (ESI Section 1.7).

Overall, we find that it is easier for a Cu_4 cluster to retain and share one or more electrons between Cu atoms on a defective $CeO_2(110)$ surface than on a stoichiometric surface, forming Cu^+ and $Cu^{\delta+}$-Cu^0 species close to the vacancy, which has been proposed as active sites for reactions such as carbonate hydrogenation [48].

4.8 Dispersion Corrections

We note from previous studies that the inclusion of dispersion corrections in the DFT+*U* based calculations has a minimal effect on the local geometrical and electronic properties [47, 49, 50]. Therefore, in this study we have only investigated the configurations which have the most negative Cu adsorption energies based on the DFT+*U* calculations, as listed in ESI Table 3, and compared the structures and energetics without (DFT+*U*) and with the van der Waals dispersion term (DFT+*U*+D3). We find that for each of the nine configurations investigated, the inclusion of the D3 term only makes the adsorption energies slightly more negative (maximum difference less than 0.23 eV) which agrees with the previous work [47, 49, 50].

4.9 Discussion

For Cu_n (n=1-4) adsorption on a stoichiometric CeO_2(110) surface, a Cu_n cluster grows along the long bridge sites until Cu_3, so that each Cu atom can strongly interact with surface oxygen ions at these sites, forming stable structures, as illustrated in Fig. 12 1-3, which, however, limits Cu-Cu interactions since they are distant from each other, hardly forming any Cu-Cu bonds. A linear Cu_3 cluster represents a component of a Cu monolayer structure on the surface, where long bridge sites are first occupied upon Cu adsorption with an increasing Cu loading. This monolayer then grows into a bilayer in a way suggested by the Cu_3 to Cu_4 transition, with long-bridge site Cu as anchoring sites. The fourth Cu either rises up from the surface (Fig. 12, 4.3) or moves down towards the surface, as illustrated in Fig. 12, 4.4, in between two adjacent long bridge sites, to bridge Cu atoms and bond with surface/subsurface oxygen ions from two adjacent long bridge sites. In this Cu monolayer to bilayer transition, Cu-Cu interactions gradually surpass in strength Cu-O interactions and become the dominant factor, resulting in Cu atoms at the top layer occupying the space in between long bridge sites and bonding with bottom-layer Cu atoms as well as surface oxygen ions; or some Cu atoms may be incorporated into the surface, as again seen in Fig. 12, 4.4, and as is observed experimentally [19, 43]. This Cu_n cluster growth pattern is also demonstrated by the trend of adsorption energy per Cu atom versus Cu_n cluster size, given in Fig. 13. From Cu_1 to Cu_2, the adsorption energy per Cu becomes more negative by ~0.2 eV to -3.492 eV, indicating a slightly more stable Cu_2 cluster than a Cu adatom on the surface, due to additional Cu-Cu interactions besides surface Cu-O interactions. The value then becomes slightly less negative at -3.429 eV at Cu_3, which then changes by ~0.5 eV at Cu_4. A similar Cu_n growth pattern is observed on a defective surface with one surface oxygen vacancy (CeO_2(110)-Ov), as illustrated in Fig. 14, except we find that the Cu adatom on the defective surface has the most negative adsorption energy. However, Cu-O interactions are significantly weakened because of oxygen vacancy formation, thus showing a less negative adsorption energy per Cu than that with a stoichiometric surface, which becomes even more substantial in the Cu_3 to Cu_4 transition, where the adsorption energy per Cu becomes less negative by ~0.7 eV.

Cu_n adsorption energy, shown in Fig. 13, suggests that growth of Cu_4 on CeO_2(110) with/out one surface oxygen vacancy is energetically less favoured, and Cu_4 is likely to dissociate to Cu_{1-3}. However, several experimental studies have reported Cu bilayers and large Cu particles on Cu/CeO_2-nanorod catalysts, prepared in solutions by wet impregnation or deposition precipitation [8, 11, 51], suggesting that under kinetic conditions, for example, adsorption sites for single Cu atoms might become unavailable, or clustering of single Cu adsorbates may destabilise individual sites to some degree, formation of larger Cu clusters can become energetically preferable.

Analysis of electronic structures of the configurations having the lowest adsorption energy clearly demonstrates electron transfer from Cu 4*s* to Ce 4*f* orbitals, readily reducing the CeO_2(110) surface both with and without a surface oxygen vacancy. A maximum of four Ce^{3+} ions are found for a Cu_n/CeO_2(110) (n=1-4) system, and a maximum of five Ce^{3+} ions for a Cu_n/CeO_2(110)-Ov (n=1-4) system. Both surface and second-layer Ce^{3+} ions are formed, but the latter is energetically less favoured. Other metastable Cu_n/CeO_2(110) structures also possess interesting electronic structures, in which either an electron pair with opposite spins or a single electron is observed on the Cu_n. For example, calculations of the metastable Cu_4/CeO_2(110)-Conf2 structure show coexistence of Cu^+, Cu^{2+}, and a topmost $Cu^{\delta-}$ species, and intriguing Cu^+/Cu^{2+} interchange at the Cu/CeO_2 interface which has been reported as providing active sites for many

reactions [6, 10, 17]. In addition, surface oxygen vacancy formation makes it easier for a Cu_4 cluster to retain and share one or more electrons between Cu atoms, forming mixed Cu^+ and $Cu^{\delta+}$-Cu^0 species close to the vacancy. The coexisting Cu^+ and Cu^0 species of a Cu bilayer at the Cu/CeO_2 interface has been proposed as actives sites for reactions such as carbonate hydrogenation [48].

By an extensive study of different possible Ce^{3+} electron spin arrangement of 38 configurations from both systems, we find that structures with an antiferromagnetic CeO_2(110) or CeO_2(110)-Ov surface are energetically favourable (see ESI Table 2) in most cases, with a maximum reduction in the adsorption energy of 0.18 eV, which strongly suggests that CeO_2(110) in both systems does not show any ferromagnetic (FM) behaviour, as reported previously [52].

A few previous studies of Cu and Cu_n adsorbed on other metal oxide surfaces, such as ZnO, MgO, TiO_2, and $SrTiO_3$, are also briefly discussed here and compared with our study. For non-reducible surfaces such as ZnO and MgO, Cu-surface metal cation interactions predominate. For example, on Zn terminated (0001) surface of ZnO, French *et al.* [53] observed that neutrally charged Cu clusters were mainly attracted to Zn cations, and that charged Cu clusters had charges mostly localised on the anchoring Cu adatom, thus showing effectively charge neutral surface copper sites. They concluded that larger copper clusters were predominantly charge neutral, as electrostatic repulsion destabilised Cu^+ ions. They [54] later reported that copper atoms in the middle layer of planar and polyhedral clusters gained a small amount of charges from surface oxygen ions. For +2 charged Cu clusters, electron transfer from oxygens to the anchoring Cu facilitated interactions between second-layer Cu and surface Zn cations, thus promoting formation of polyhedral Cu clusters, with the formed Cu^{x+} sites being the nucleation centres. Mora-Fonz *et al.* [55] reported Cu adsorption energy on non-polar $(10\bar{1}0)$ surface of ZnO, in a range of 0.365-1.981 eV. On reconstructed polar Zn-terminated (0001) and O-terminated $(000\bar{1})$ surface, Higham *et al.* [56] found that planar and 3D Cu cluster growth were favoured, respectively, because of strong attractive Cu-Zn and repulsive Cu-O interactions. On the O-rich Zn-terminated reconstructed surface, they also observed close interaction between Cu and surface oxygens, with electron transfer from coordinating Cu atoms to surface O ions.

Pacchioni and Rösch [57] found that Cu-Cu interactions were stronger than Cu-surface interactions, in Cu_4 adsorption on MgO(110). Cu and Cu_4 were weakly oxidised by surface oxygens, showing a weak polar covalent bond with limited charge transfer from Cu 4*s* to surface O 2*p*, with adsorption energies of 0.34 and 0.36 eV, respectively. Geudtner et al. [58] later revealed that Cu-Cu interactions were the dominating factor in larger Cu_n (n=2-6) cluster formation on MgO(100), stronger than Cu-surface oxygen interactions, with reported adsorption energies of 1.91-2.31 eV.

For Cu adsorption on reducible surfaces such as TiO_2, it was reported that Cu adatom bound strongly to TiO_2(110) nearer to surface bridging O ions [59], and that a Cu_7 cluster retained its pentagonal bipyramidal structure on TiO_2 surface, because of strong Cu-O and weak Cu-Ti interactions [60, 61]. Natile *et al.* [62] reported Cu_2 adsorption on $SrTiO_3$(100) with an adsorption energy of -1.74 eV, and observed strong interactions between Cu and surface oxygens.

Ceria is highly reducible, and electron transfer from Cu_n to surface Ce^{4+} is clearly observed upon Cu_n adsorption on CeO_2(110), which, is very different from that on non-reducible surfaces such as ZnO and MgO, where Cu-surface metal cation interactions predominate, with a small amount of charge transfer either from Cu clusters to surface oxygens or vice versa, depending on the exact model studied. Yet, our detailed study of small Cu_n (n=1-4) cluster adsorption on CeO_2(110) agrees in general with the aforementioned studies of TiO_2, that copper-metal oxide interactions are

important in determining geometry and stability of Cu/metal oxide structures [60]. The calculated adsorption energies of Cu_n on CeO_2(110), absolute values of 2.971-3.492 eV, are generally higher than the abovementioned values for other surfaces, suggesting strong interactions between copper and ceria. In addition, experimental studies reported that nanostructured Cu/CeO_2 catalysts had a copper particle size-activity dependence [51], which thus strongly stimulates further study of larger Cu cluster adsorption on CeO_2(110).

5. Conclusions

The atomic and electronic structures of a Cu_n (n=1-4) cluster adsorbed on either a stoichiometric CeO_2(110) surface or a defective surface with one oxygen vacancy (CeO_2-Ov) have been investigated by DFT calculations without using pre-assumed Cu_n cluster shapes. Both the stoichiometric and defective surface are readily reduced upon Cu_n adsorption, forming surface and second-layer Ce^{3+} ions, and do not show any FM behaviour. On both surfaces, Cu_1 grows to Cu_3 along the long bridge sites, forming strong Cu-O bonds at adjacent long bridge sites, which models a Cu monolayer growth mechanism. The Cu_3 to Cu_4 transition suggests that this monolayer then begins to grow into a bilayer, with long-bridge site Cu as anchoring sites, where top-layer Cu atoms [11] occupy the space in between long bridge sites to bond strongly with bottom-layer Cu and surface oxygens; or some Cu atoms are incorporated into the CeO_2(110) surface lattice, as observed experimentally [19, 43]. Surface oxygen vacancy formation however weakens Cu-O interactions at the surface, thus making Cu adsorption energy less negative.

A Cu bilayer is rich in Cu^+ species at the Cu-O interface (four Cu^+ in Cu_4/CeO_2, two Cu^+ and two $Cu^{\delta+}$ in Cu_4/CeO_2-Ov), agreeing with experimental results [11]. In metastable structures, it also shows Cu^{2+} and $Cu^{\delta-}$ species, and $Cu^{\delta+}$-Cu^0 species on a stoichiometric and a defective surface, respectively. This interesting Cu^{2+}/Cu^+ and Cu^+/Cu^0 interplay observed in our work thus give a theoretical basis to many experimental studies where the Cu^{2+}/Cu^+ pair and the Cu^+/Cu^0 pair were proposed as active sites for CuO_x/CeO_2-nanorod catalysts in many reactions [6, 10, 17, 48]. In the future work we will explore the structures and energetics of larger Cu clusters adsorbed on the CeO_2(110) surface.

6. Supporting Information

The supporting Information is available free of charge at http://...

Cartesian coordinates of all the optimised structures of the Cu_n(n=1-4)/CeO_2(110) and Cu_n(n=1-4)/CeO_2(110)-Ov system from both DFT+U and DFT+U+D3 calculations can be found here (ZIP).

7. Acknowledgements

Rui Zhang thanks the Department of Chemical Engineering, Imperial College London for the award of a Department Scholarship. This study was initiated under the EPSRC Low Carbon Fuels programme EP/N009533/1 & EP/N010531/1. We thank Dr Richardo Grau-Crespo for his helpful discussions on modelling the Ce^{4+} to Ce^{3+} reduction process. We also thank Dr David Mora-Fonz for his helpful discussions and suggestions. This work used the computing resources from the ARCHER UK National Super-computing Service http://www.archer.ac.uk/, the THOMAS and the YOUNG UK National Tier 2 Super-computing Service, via our membership of the UK's HEC Materials Chemistry Consortium (MCC), which is funded by EPSRC (EP/L000202). This work also used the UK Materials and Molecular Modelling Hub for computational resources, MMM Hub, which is partially funded by EPSRC (EP/P020194 and EP/T022213). We also thank UCL for access to the KATHLEEN and Faraday computing facilities. We also acknowledge the use of HPC Midlands Plus (funded by the EPSRC (grant EP/P020232/1) and Cirrus (funded by the University of Edinburgh and EPSRC(EP/PO20267/1)).

8. References

1. T. Montini, M. Melchionna, M. Monai and P. Fornasiero, *Chem Rev*, 2016, **116**, 5987-6041.
2. J. Paier, C. Penschke and J. Sauer, *Chem Rev*, 2013, **113**, 3949-3985.
3. J. Kaspar, P. Fornasiero and M. Graziani, *Catalysis Today*, 1999, **50**, 285-298.
4. A. Trovarelli, *Catalysis Reviews*, 1996, **38**, 439-520.
5. W.-W. Wang, W.-Z. Yu, P.-P. Du, H. Xu, Z. Jin, R. Si, C. Ma, S. Shi, C.-J. Jia and C.-H. Yan, *ACS Catalysis*, 2017, **7**, 1313-1329.
6. M. Zabilskiy, P. Djinović, E. Tchernychova, O. P. Tkachenko, L. M. Kustov and A. Pintar, *ACS Catalysis*, 2015, **5**, 5357-5365.
7. H. X. Mai, L. D. Sun, Y. W. Zhang, R. Si, W. Feng, H. P. Zhang, H. C. Liu and C. H. Yan, *J. Phys. Chem. B*, 2005, **109**, 24380-24385.
8. A. Chen, X. Yu, Y. Zhou, S. Miao, Y. Li, S. Kuld, J. Sehested, J. Liu, T. Aoki, S. Hong, M. F. Camellone, S. Fabris, J. Ning, C. Jin, C. Yang, A. Nefedov, C. Wöll, Y. Wang and W. Shen, *Nature Catalysis*, 2019, **2**, 334-341.
9. S. Y. Yao, W. Q. Xu, A. C. Johnston-Peck, F. Z. Zhao, Z. Y. Liu, S. Luo, S. D. Senanayake, A. Martı´nez-Arias, W. J. Liu and J. A. Rodriguez, *Phys.Chem.Chem.Phys.*, 2014, **16**, 17183-17195.
10. L. Kang, B. Wang, Q. Bing, M. Zalibera, R. Buchel, R. Xu, Q. Wang, Y. Liu, D. Gianolio, C. C. Tang, E. K. Gibson, M. Danaie, C. Allen, K. Wu, S. Marlow, L. D. Sun, Q. He, S. Guan, A. Savitsky, J. J. Velasco-Velez, J. Callison, C. W. M. Kay, S. E. Pratsinis, W. Lubitz, J. Y. Liu and F. R. Wang, *Nat Commun*, 2020, **11**, 4008.
11. J. Ning, C. Dong, M. Li, Y. Zhou and W. Shen, *The Journal of Chemical Physics*, 2020, **152**, 094708.
12. J. C. Conesa, *Surface Science*, 1995, **339**, 337-352.
13. L. Szabová, M. F. Camellone, M. Huang, V. Matolin and S. Fabris, *J Chem Phys*, 2010, **133**, 234705.
14. Z. Yang, L. Xie, D. Ma and G. Wang, *The Journal of Physical Chemistry C*, 2011, **115**, 6730-6740.
15. L. O. Paz-Borbon, F. Buendia, I. L. Garzon, A. Posada-Amarillas, F. Illas and J. Li, *Phys Chem Chem Phys*, 2019, **21**, 15286-15296.
16. J. F. Jerratsch, X. Shao, N. Nilius, H. J. Freund, C. Popa, M. V. Ganduglia-Pirovano, A. M. Burow and J. Sauer, *Phys Rev Lett*, 2011, **106**, 246801.
17. S. Yao, K. Mudiyanselage, W. Xu, A. C. Johnston-Peck, J. C. Hanson, T. Wu, D. Stacchiola, J. A. Rodriguez, H. Zhao, K. A. Beyer, K. W. Chapman, P. J. Chupas, A. Martínez-Arias, R. Si, T. B. Bolin, W. Liu and S. D. Senanayake, *ACS Catalysis*, 2014, **4**, 1650-1661.
18. L. Lin, S. Yao, Z. Liu, F. Zhang, N. Li, D. Vovchok, A. Martínez-Arias, R. Castañeda, J. Lin, S. D. Senanayake, D. Su, D. Ma and J. A. Rodriguez, *The Journal of Physical Chemistry C*, 2018, **122**, 12934-12943.
19. L. Liu, Z. Yao, Y. Deng, F. Gao, B. Liu and L. Dong, *ChemCatChem*, 2011, **3**, 978-989.
20. M. Nolan, *J Chem Phys*, 2012, **136**, 134703.
21. L. Cui, Y. Tang, H. Zhang, L. G. Hector, Jr., C. Ouyang, S. Shi, H. Li and L. Chen, *Phys Chem Chem Phys*, 2012, **14**, 1923-1933.
22. A. Chutia, E. K. Gibson, M. R. Farrow, P. P. Wells, D. O. Scanlon, N. Dimitratos, D. J. Willock and C. R. A. Catlow, *Phys Chem Chem Phys*, 2017, **19**, 27191-27203.
23. Z. Ren, N. Liu, B. Chen, J. Li and D. Mei, *The Journal of Physical Chemistry C*, 2018, **122**, 27402-27411.
24. J. Kullgren, K. Hermansson and C. Castleton, *J Chem Phys*, 2012, **137**, 044705.
25. G. Kresse and J. Hafner, *Phys Rev B Condens Matter*, 1993, **47**, 558-561.
26. G. Kresse and J. Hafner, *Phys Rev B Condens Matter*, 1994, **49**, 14251-14269.
27. G. Kresse and J. Furthmüller, *Physical Review B*, 1996, **54**, 11169-11186.

28. P. E. Blöchl, *Phys Rev B Condens Matter*, 1994, **50**, 17953-17979.
29. J. P. Perdew, K. Burke and M. Ernzerhof, *Physical Review Letters*, 1996, **77**, 3865-3868.
30. G. Makov and M. C. Payne, *Phys Rev B Condens Matter*, 1995, **51**, 4014-4022.
31. J. Neugebauer and M. Scheffler, *Phys Rev B Condens Matter*, 1992, **46**, 16067-16080.
32. H. J. Monkhorst and J. D. Pack, *Physical Review B*, 1976, **13**, 5188-5192.
33. V. V. Anisimov, J. Zaanen and O. K. Andersen, *Phys Rev B Condens Matter*, 1991, **44**, 943-954.
34. V. V. Anisimov, I. I. Solovyev, M. A. Korotin, M. T. Czyzyk and G. A. Sawatzky, *Phys Rev B Condens Matter*, 1993, **48**, 16929-16934.
35. I. I. Solovyev, P. H. Dederichs and V. V. Anisimov, *Phys Rev B Condens Matter*, 1994, **50**, 16861-16871.
36. S. L. Dudarev, G. A. Botton, S. Y. Savrasov, C. J. Humphreys and A. P. Sutton, *Physical Review B*, 1998, **57**, 1505-1509.
37. H. Raebiger, S. Lany and A. Zunger, *Physical Review B*, 2007, **76**.
38. E. L. Wilson, R. Grau-Crespo, C. L. Pang, G. Cabailh, Q. Chen, J. A. Purton, C. R. A. Catlow, W. A. Brown, N. H. de Leeuw and G. Thornton, *J. Phys. Chem. C*, 2008, **112**, 10918–10922.
39. N. C. Hernández, R. Grau-Crespo, N. H. de Leeuw and J. F. Sanz, *Phys Chem Chem Phys*, 2009, **11**, 5246-5252.
40. M. M. Branda, N. J. Castellani, R. Grau-Crespo, N. H. de Leeuw, N. C. Hernandez, J. F. Sanz, K. M. Neyman and F. Illas, *J Chem Phys*, 2009, **131**, 094702.
41. W. Tang, E. Sanville and G. Henkelman, *J Phys Condens Matter*, 2009, **21**, 084204.
42. K. Momma and F. Izumi, *Journal of Applied Crystallography*, 2011, **44**, 1272-1276.
43. D. Gamarra, A. L. Cámara, M. Monte, S. B. Rasmussen, L. E. Chinchilla, A. B. Hungría, G. Munuera, N. Gyorffy, Z. Schay, V. C. Corberán, J. C. Conesa and A. Martínez-Arias, *Applied Catalysis B: Environmental*, 2013, **130-131**, 224-238.
44. Z. Yang, T. K. Woo, M. Baudin and K. Hermansson, *J Chem Phys*, 2004, **120**, 7741-7749.
45. S. Fabris, G. Vicario, G. Balducci, S. de Gironcoli and S. Baroni, *J. Phys. Chem. B*, 2005, **109**, 22860-22867.
46. M. Nolan, D. G. Parker and G. W. Watson, *Surface Science*, 2005, **595**, 223-232.
47. A. Chutia, D. J. Willock and C. R. A. Catlow, *Faraday Discuss*, 2018, **208**, 123-145.
48. Y. Cui and W.-L. Dai, *Catalysis Science & Technology*, 2016, **6**, 7752-7762.
49. L. Chen, T. V. W. Janssens and H. Gronbeck, *Phys Chem Chem Phys*, 2019, **21**, 10923-10930.
50. M. Delarmelina, M. G. Quesne and C. R. A. Catlow, *Phys Chem Chem Phys*, 2020, **22**, 6660-6676.
51. J. Zhu, Y. Su, J. Chai, V. Muravev, N. Kosinov and E. J. M. Hensen, *ACS Catalysis*, 2020, **10**, 11532-11544.
52. P. R. Keating, D. O. Scanlon and G. W. Watson, *J Phys Condens Matter*, 2009, **21**, 405502.
53. S. A. French, A. A. Sokol, S. T. Bromley, C. R. A. Catlow and P. Sherwood, *Topics in Catalysis*, 2003, **24**.
54. S. A. French, A. A. Sokol, C. R. A. Catlow and P. Sherwood, *J. Phys. Chem. C*, 2008, **112**, 7420-7430.
55. D. Mora-Fonz, T. Lazauskas, S. M. Woodley, S. T. Bromley, C. R. A. Catlow and A. A. Sokol, *The Journal of Physical Chemistry C*, 2017, **121**, 16831-16844.
56. M. D. Higham, D. Mora-Fonz, A. A. Sokol, S. M. Woodley and C. R. A. Catlow, *Journal of Materials Chemistry A*, 2020, **8**, 22840-22857.
57. G. Pacchioni and N. Rösch, *J. Chem. Phys.*, 1996, **104**, 7329.
58. G. Geudtner, K. Jug and A. M. Köster, *Surface Science*, 2000, **467**, 98-106.
59. D. Pillay, Y. Wang and G. S. Hwang, *Korean J. Chem. Eng.*, 2004, **21**, 537-547.

View Article Online
DOI: 10.1039/D1CP02973H

60. S. M. Shearin, *Modern Concepts in Material Science*, 2020, **2**.
61. Y. Lan, Y. Xie, J. Chen, Z. Hu and D. Cui, *Chem Commun (Camb)*, 2019, **55**, 8068-8071.
62. M. M. Natile, S. Carlotto, G. Bizzotto, A. Vittadini and A. Glisenti, *European Journal of Inorganic Chemistry*, 2018, **2018**, 3829-3834.

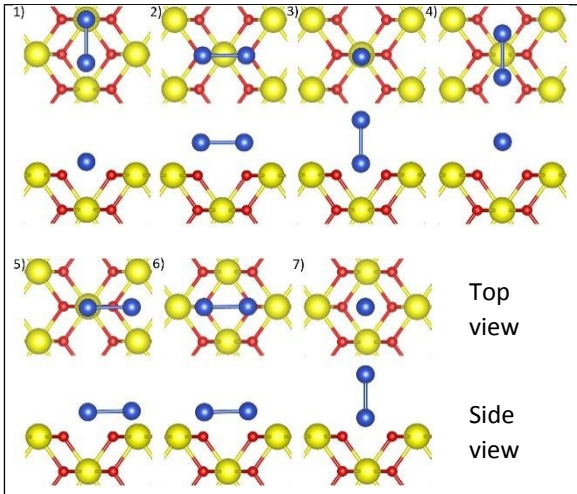

Figure 1: Top view and side view of seven initial configurations of a Cu_2 cluster placed at different adsorption sites on the $CeO_2(110)$ surface, labelled as 1) to 7). Cerium, oxygen, and copper atoms are represented by red, yellow, and blue spheres respectively.

View Article Online
DOI: 10.1039/D1CP02973H

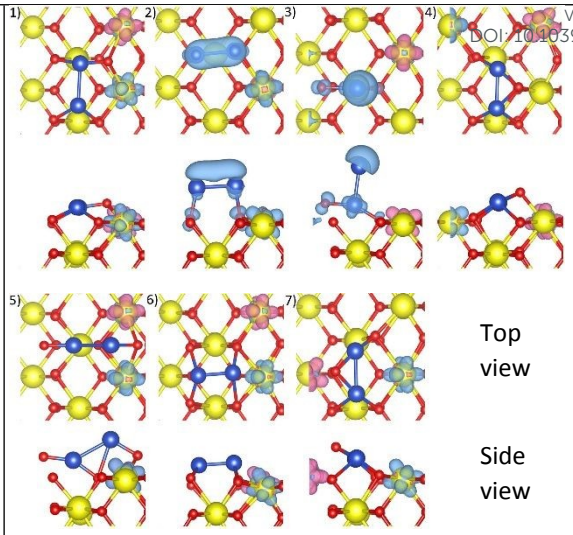

Figure 2: Top view and side view of optimised $Cu_2/CeO_2(110)$ structures with spin density isosurfaces of 0.005 eÅ^{-3} around Cu and reduced Ce^{3+} ions, labelled as 1) to 7). Blue: up spin; Pink: down spin.

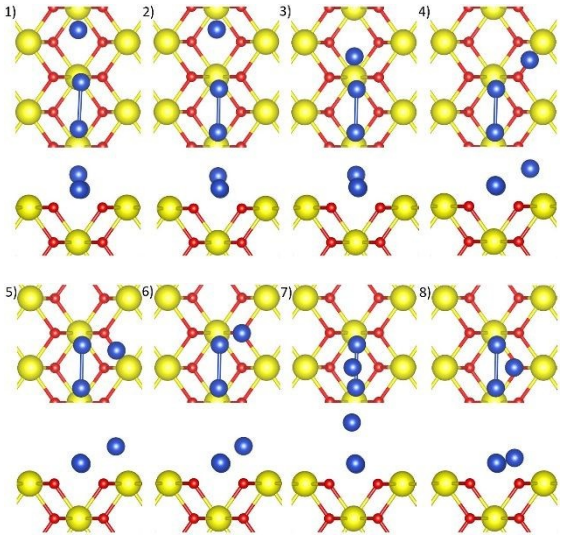

Figure 3: Top and side view of eight initial configurations of a Cu_3 cluster located at different adsorption sites on the $CeO_2(110)$ surface, labelled as 1) to 8). The Cu_2 clusters are emphasised by the Cu-Cu bond.

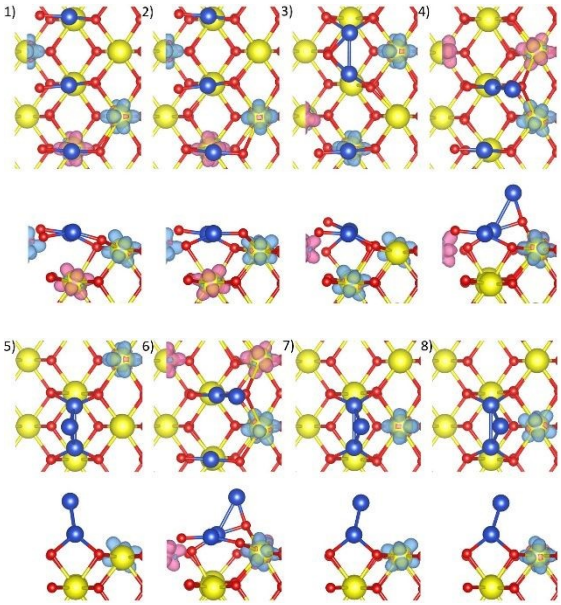

Figure 4: Top view and side view of optimised $Cu_3/CeO_2(110)$ structures with spin density isosurfaces of 0.005 eÅ^{-3} around Cu and reduced Ce^{3+} ions, labelled as 1) to 8).

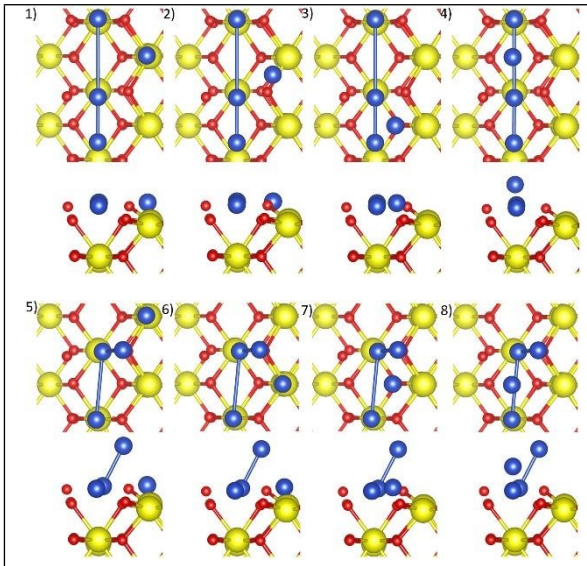

Figure 5: Top view and side view of eight initial configurations of a Cu_4 cluster located at different adsorption sites on the $CeO_2(110)$ surface, labelled as 1) to 8). The Cu_3 clusters are emphasised by the Cu-Cu bonds which may not physically exist.

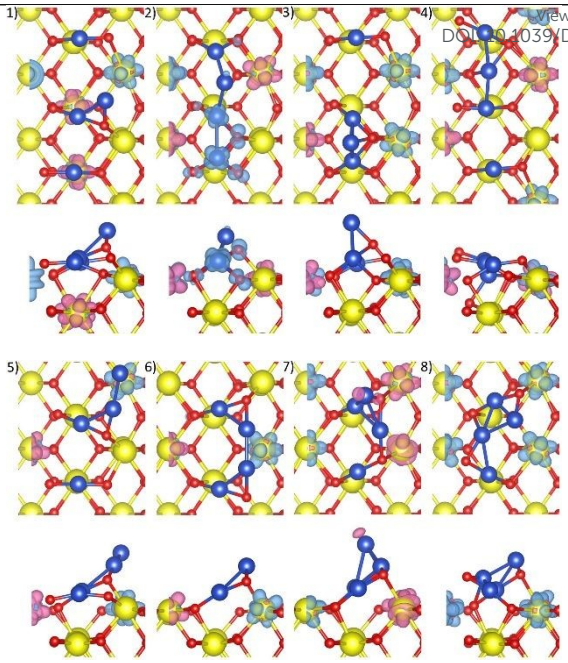

Figure 6: Top view and side view of optimised $Cu_4/CeO_2(110)$ structures with the spin density isosurfaces of 0.005 $eÅ^{-3}$ around Cu and reduced Ce^{3+} ions, labelled as 1) to 8).

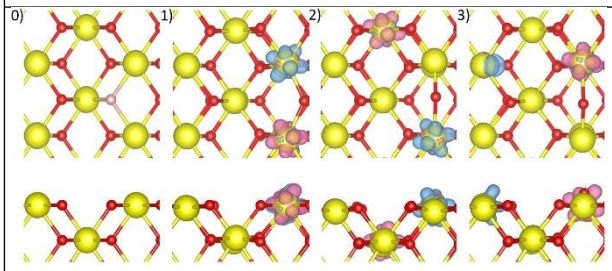

Figure 7: Top view and side view of 0) an initial structure of $CeO_2(110)$-Ov surface (the removed oxygen atom is highlighted using a light pink sphere); 1)-3) three optimised $CeO_2(110)$ surface structures with spin density isosurfaces of 0.005 $eÅ^{-3}$ around reduced Ce^{3+} ions which are located at different positions on the surface.

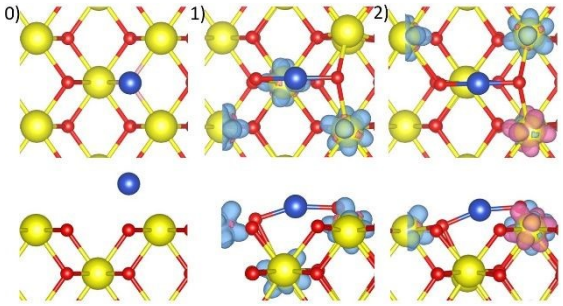

Figure 8: Top view and side view of 0) the initial structure of the O_{top} configuration from the $Cu/CeO_2(110)$ system with one oxygen vacancy; 1)-2) two optimised structures with spin density isosurfaces of 0.005 $eÅ^{-3}$ around reduced Ce^{3+} ions which are located at different positions on the surface.

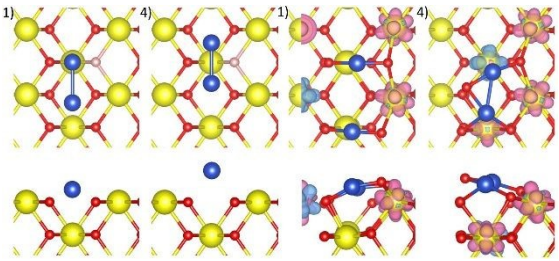

Figure 9: Top view and side view of Left 1) and 4): the initial structure of Conf1v and 4v, respectively, from the $Cu_2/CeO_2(110)$ system with one oxygen vacancy; Right 1) and 4) the corresponding optimised structures of Conf1v and 4v with spin density isosurfaces of 0.005 $eÅ^{-3}$ around Cu and reduced Ce^{3+} ions.

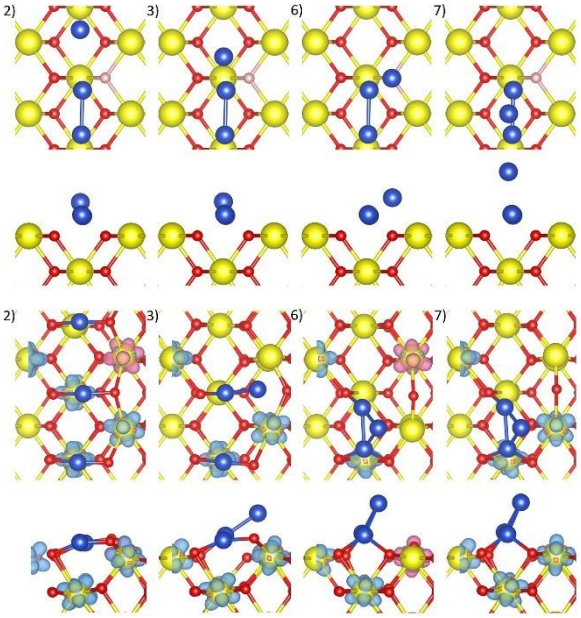

Figure 10: Top row: top view and side view of initial structures of Conf1v, 2v, 6v and 7v, respectively, from the $Cu_3/CeO_2(110)$ system with one oxygen vacancy. The Cu_2 clusters are emphasised by the Cu-Cu bond. Bottom row: Top view and side view of the corresponding optimised structures of Conf1v, 2v, 6v and 7v, respectively, with spin density isosurfaces of 0.005 $eÅ^{-3}$ around Cu and reduced Ce^{3+} ions.

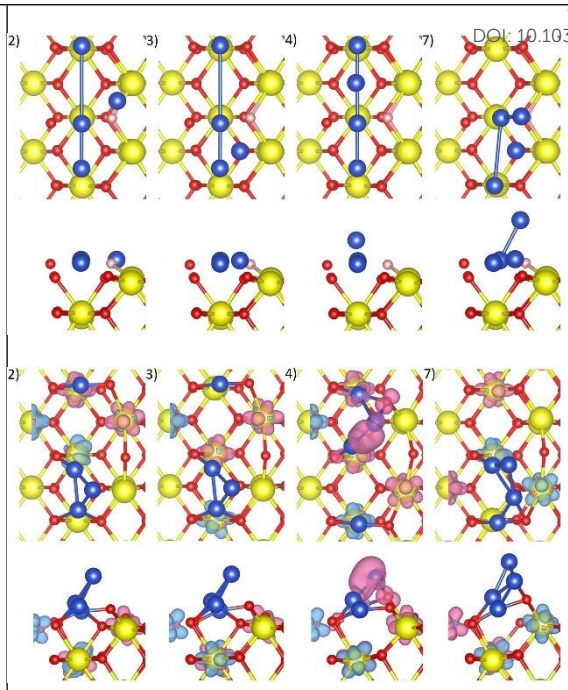

Figure 11: Top row: top view and side view of initial structures of Conf2v, 3v, 4v and 7v, respectively, from the $Cu_4/CeO_2(110)$ system with one oxygen vacancy. The Cu_3 clusters are emphasised by the Cu-Cu bonds which may not physically exist. Bottom row: Top view and side view of the corresponding optimised structures of Conf2v, 3v, 4v and 7v, respectively, with spin density isosurfaces of 0.005 $eÅ^{-3}$ around Cu and reduced Ce^{3+} ions.

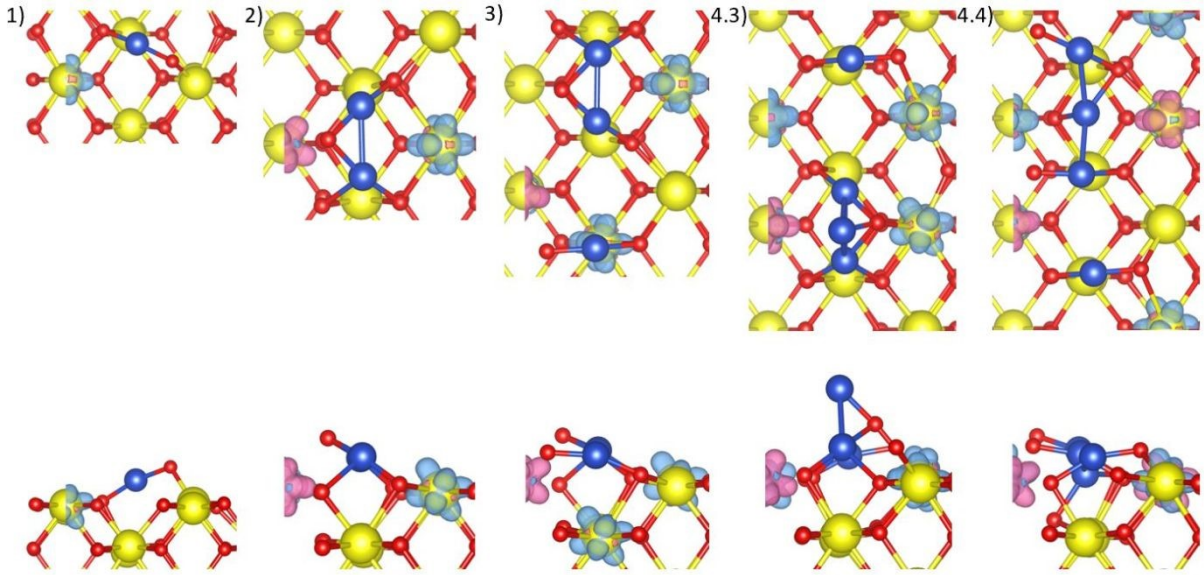

Figure 12: Top view and side view of the most stable $Cu_n/CeO_2(110)$ (n=1-4) structures, labelled as 1) to 4); 4.3) and 4.4) are the optimised structures of Conf3 and 4, respectively, which have almost the same stability.

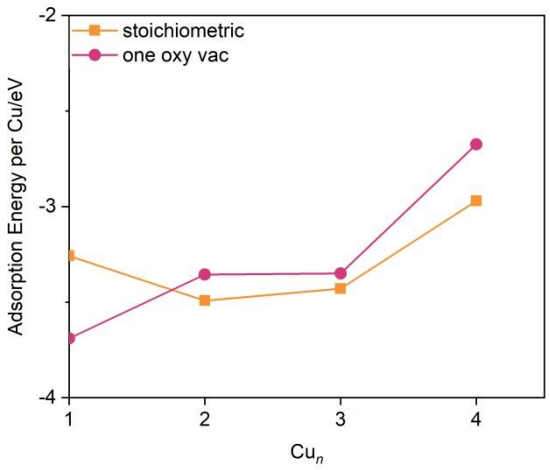

Figure 13: Adsorption energy per Cu atom as a function of the Cu_n cluster size on a stoichiometric and a defective CeO_2(110) surface with one oxygen vacancy, respectively.

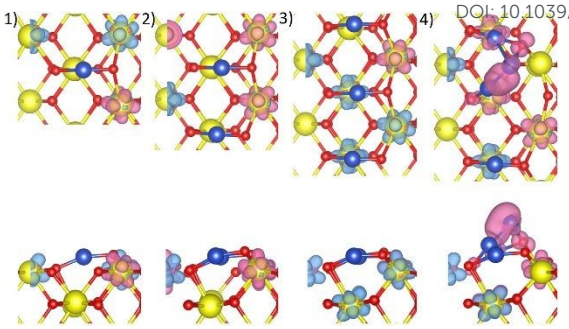

Figure 14: Top view and side view of the most stable Cu_n/CeO_2(110)-Ov (n=1-4) structures with the spin density isosurfaces of 0.005 $eÅ^{-3}$ around Cu and reduced Ce^{3+} ions, labelled as 1) to 4).

View Article Online
DOI: 10.1039/D1CP02973H

Table 1: $Cu_2/CeO_2(110)$ system: calculated magnetic moment of Cu clusters (s, p, d orbitals) and individual Ce^{3+} ions (s, p, d, f orbitals) in Bohr magneton (μ_B); number of Ce^{3+} ions; average Cu-O bond length shown in Fig. 2 (Å); Cu-Cu bond length (Å); average Ce-O bond length (Å) on the surface; adsorption energy per Cu atom (eV).

System	$M_{Cu\ cluster}$ (μ_B)	M_{Ce} (μ_B)	Number of Ce^{3+} reduced	Cu-O (Å)	Cu-Cu (Å)	$(Ce\text{-}O)_{surf}$ (Å)	E_{ad} (eV)
Conf1	0	0.941/-0.969	2	1.846	2.601	2.360	-2.810
Conf2	0.329	0.966	1	1.834	2.268	2.349	-1.725
Conf3	0.326	-0.968	1	1.781	2.342	2.352	-2.054
Conf4	0	0.966/-0.963	2	1.904	2.411	2.342	-3.367
Conf5	0	0.952/-0.952	2	1.936	2.512	2.367	-2.163
Conf6	0.022	0.859/-0.964	2	2.033	2.175	2.369	-0.973
Conf7	0	0.968/-0.966	2	1.908	2.478	2.345	-3.492

Table 2: $Cu_3/CeO_2(110)$ system: calculated magnetic moment of Cu clusters (s, p, d orbitals) and individual Ce^{3+} ions (s, p, d, f orbitals) in Bohr magneton (μ_B); number of Ce^{3+} ions; average Cu-O bond length shown in Fig. 8 (Å); average Cu-Cu bond length (Å); average Ce-O bond length (Å) on the surface; adsorption energy per Cu atom (eV).

System	$M_{Cu\ cluster}$ (μ_B)	M_{Ce} (μ_B)	Number of Ce^{3+} reduced	Cu-O (Å)	Cu-Cu (Å)	$(Ce\text{-}O)_{surf}$ (Å)	E_{ad} (eV)
Conf1	0	0.969/0.972/-0.967	3	1.778	--	2.357	-3.307
Conf2	0	0.970/0.974/-0.964	3	1.781	--	2.455	-3.318
Conf3	0	0.960/0.966/-0.970	3	1.872	2.463	2.347	-3.429
Conf4	0	0.966/-0.967/-0.935	3	1.784	2.532	2.377	-2.779
Conf5	0	0.968	1	1.959	2.368	2.351	-2.715
Conf6	0	0.963/-0.959/-0.968	3	1.779	2.531	2.372	-2.810
Conf7	0	0.967	1	1.963	2.381	2.351	-2.720
Conf8	0	0.964	1	1.963	2.382	2.351	-2.605

View Article Online
DOI: 10.1039/D1CP02973H

Table 3: $Cu_4/CeO_2(110)$ system: calculated magnetic moment of Cu clusters (s, p, d orbitals), of all Ce^{3+} ions and individual Ce^{3+} ions (s, p, d, f orbitals) in Bohr magneton (μ_B); number of Ce^{3+} ions; average Cu-O bond length shown in Fig. 11 (Å); average Cu-Cu bond length (Å); average Ce-O bond length (Å) on the surface; adsorption energy per Cu atom (eV).

System	$M_{Cu\ cluster}$ (μ_B)	$M_{Ce\text{-}total}$ (μ_B)	M_{Ce} (μ_B)	Number of Ce^{3+} reduced	Cu-O (Å)	Cu-Cu (Å)	$(Ce\text{-}O)_{surf}$ (Å)	E_{ad} (eV)
Conf1	0.006	-0.009	0.958/0.952/ -0.961/-0.958	4	1.790	2.516	2.346	-2.918
Conf2	0.577	-0.954	0.967/-0.967/ -0.954	3	1.894	2.428	2.352	-2.859
Conf3	-0.007	1.925	0.945/0.966/ 0.965/-0.951	4	1.868	2.495	2.369	-2.971
Conf4	0	0.009	0.970/0.968/ -0.964/-0.965	4	1.844	2.417	2.364	-2.961
Conf4-2	0.303	-0.941	0.970/-0.949/ -0.962	3	1.914	2.361	2.353	-2.840
Conf5	0	0	0.964/-0.968	2	1.785	2.441	2.338	-2.470
Conf6	-0.041	-0.020	0.949/-0.969	2	1.851	2.488	2.334	-2.752
Conf7	-0.064	0.210	-0.755/0.970/ 0.966/0.969	4	1.828	2.560	2.361	-2.806
Conf8	0	0.008	0.957/0.957/ -0.942/-0.964	4	1.860	2.410	2.356	-2.792

Table 4: $CeO_2(110)$-Ov system: calculated magnetic moment of individual Ce^{3+} ions (s, p, d, f orbitals) in Bohr magneton (μ_B); number of Ce^{3+} ions reduced; average Ce-O bond length (Å) on the surface and in the two sublayers, as shown in Fig. 16; oxygen vacancy formation energy (eV).

System	M_{Ce} (μ_B)	Number of Ce^{3+} reduced	$(Ce\text{-}O)_{surf}$ (Å)	$(Ce\text{-}O)_{sub}$ (Å)	E_v (eV)
Case1	0.969/-0.973	2	2.338	2.381	1.110
Case2	0.962/-0.899	2	2.329	2.374	1.426
Case3	-0.966/0.946	2	2.333	2.373	0.978

View Article Online
DOI: 10.1039/D1CP02973H

Table 5: $Cu/CeO_2(110)$-Ov system (Case1, 2) and $Cu_2/CeO_2(110)$-Ov system (Conf1v, 4v): calculated total magnetic moment of the optimised structures and that of individual Ce^{3+} ions (*s*, *p*, *d*, *f* orbitals) in Bohr magneton (μB); number of Ce^{3+} ions reduced; average Cu-O bond length shown in Fig. 17 and 18, respectively (Å); average Ce-O bond length (Å) on the surface; adsorption energy per Cu atom (eV).

System	M_{total} (μ_B)	M_{Ce} (μ_B)	Number of Ce^{3+} reduced	Cu-O (Å)	Cu-Cu (Å)	$(Ce\text{-}O)_{surf}$ (Å)	E_{ad} (eV)
Case1	2.896	0.969/0.955/0.973	3	1.818	--	2.343	-3.595
Case2	0.974	0.969/0.972/-0.967	3	1.809	--	2.349	-3.690
Conf1v	-1.937	-0.975/-0.971/0.967/-0.960	4	1.793	--	2.360	-3.356
Conf4v	-1.929	-0.972/-0.971/-0.950/0.963	4	1.908	2.479	2.317	-3.207

Table 6: $Cu_3/CeO_2(110)$-Ov and $Cu_4/CeO_2(110)$-Ov system: calculated total magnetic moment of the optimised structures and that of individual Ce^{3+} ions (s, p, d, f orbitals) in Bohr magneton (μ_B); number of Ce^{3+} ions; average Cu-O bond length shown in Fig. 19, 21, respectively (Å); average Cu-Cu bond length (Å); average Ce-O bond length (Å) on the surface; adsorption energy per Cu atom (eV).

System	M_{total} (μ_B)	M_{Ce} (μ_B)	Number of Ce^{3+} reduced	Cu-O (Å)	Cu-Cu (Å)	$(Ce\text{-}O)_{surf}$ (Å)	E_{ad} (eV)
$Cu_3/CeO_2(110)$-Ov							
Conf2v	2.896	0.975/-0.975/0.969/ 0.964/0.964	5	1.795	--	2.351	-3.350
Conf3v	2.898	0.971/0.969/0.959	3	1.796	2.258	2.345	-2.420
Conf6v	0.948	-0.972/0.969/0.952	3	1.910	2.355	2.347	-2.557
Conf7v	2.888	0.971/0.969/0.950	3	1.911	2.360	2.342	-2.575
$Cu_4/CeO_2(110)$-Ov							
Conf2v	-0.106	-0.972/0.967/0.856/ -0.956	4	1.860	2.353	2.342	-2.495
Conf3v	0	-0.968/0.967/0.952/ -0.953	4	1.861	2.357	2.341	-2.586
Conf4v	-1.381	-0.974/0.965/0.962/ -0.964/-0.961	5	1.810	2.451	2.336	-2.674
Conf7v	0	0.972/-0.967/0.963/ -0.958	4	1.803	2.390	2.351	-2.574